PHYSICAL REVIEW B **98**, 125107 (2018)

Pairing mechanism for nodal s-wave superconductivity in BaFe$_2$(As, P)$_2$: Analysis beyond Migdal-Eliashberg formalism

Hironori Nakaoka, Youichi Yamakawa, and Hiroshi Kontani
Department of Physics, Nagoya University, Furo-cho, Nagoya 464-8602, Japan

(Received 28 May 2018; revised manuscript received 27 July 2018; published 5 September 2018)

The pairing mechanism and gap structure in Ba122 pnictides have been hotly discussed for a long time as one of the central issues in Fe-based superconductors. Here, we attack this problem by taking account of the vertex corrections (VCs) for the Coulomb interaction U (U-VCs), which are totally dropped in conventional Migdal-Eliashberg formalism. The U-VC in the charge susceptibility induces strong orbital fluctuations, and the U-VC enlarges the orbital-fluctuation-driven attractive interaction. By analyzing the effective multiorbital Hubbard model for Ba122 pnictides, we find that the orbital fluctuations develop in all four d orbitals (t_{2g} and z^2 orbitals) by which the Fermi surfaces (FSs) are composed. For this reason, nearly isotropic gap functions appear on all the hole-type FSs, including the outer hole FS around the Z point composed of the z^2 orbital. In contrast, nodal gap structure appears on the electron FSs for the wide parameter range. The obtained nodal s-wave state changes to a fully gapped s-wave state without sign reversal (s_{++}-wave state) by introducing a small amount of impurities, accompanied by a small reduction in T_c. The present microscopic theory naturally explains the important characteristics of the gap structure of both hole and electron FSs in Ba122 pnictides without introducing any phenomenological pairing interaction.

DOI: 10.1103/PhysRevB.98.125107

I. INTRODUCTION

Ba122 pnictides have been studied for a long time as typical Fe-based superconductors, which are strongly correlated multiorbital superconductors. As possible pairing states, both the spin-fluctuation-mediated $s_\pm$-wave state [1–4] and the orbital-fluctuation-mediated s_{++}-wave state [5] have been discussed in various Fe-based superconductors. In many compounds, the hole and electron Fermi surfaces (FSs) are composed of only three t_{2g} orbitals; xz, yz, and xy orbitals. In the case of Ba122 compounds, the z^2 orbital contributes to the outer cylinder hole FS around the Z point in addition to t_{2g} orbitals. There is no z^2-orbital weight on electron FSs. The superconducting gap function on the z^2-orbital outer hole FS has been analyzed for years as a key to understand the pairing mechanism [6–10].

When the random-phase approximation (RPA) was applied to the three-dimensional Ba122 system [6], spin fluctuations develop only in the t_{2g} orbitals, whereas spin fluctuations in the z^2 orbital remain very small due to the absence of interpocket nesting. For this reason, in the obtained $s_\pm$-wave state, the gap function of the z^2-orbital outer hole FS Δ_{h,z^2} is small. Thus, the horizontal node appears robustly within the RPA. However, several angle-resolved photoemission spectroscopy (ARPES) studies [7,8] reported the absence of the horizontal node, that is, the relation $\Delta_{h,z^2} \sim \Delta_{h,t_{2g}}$ holds. In contrast, the presence of the horizontal node ($\Delta_{h,z^2}\Delta_{h,t_{2g}} < 0$ and $|\Delta_{h,z^2}| \ll \Delta_{h,t_{2g}}$) was reported in Ref. [9]. To understand the relation $\Delta_{h,z^2} \sim \Delta_{h,t_{2g}}$, the present authors showed that the nearly orbital-independent fully gapped s_{++}-wave state is realized on all hole FSs when strong interorbital fluctuations involving four d orbitals emerge [10]. Thus, the presence or absence of the horizontal node in Ba122 is a significant key factor to distinguish the pairing mechanism.

To clarify the pairing mechanism, it is significant to understand the origin of the electronic nematic order at T_S, which is above the magnetic order temperature T_N. Both the spin-nematic scenario [11,12] and the orbital order scenario [13–16] have been discussed very actively. In the latter scenario, higher-order electronic correlations, called the vertex corrections (VCs), should be taken into account. In Ref. [15], the authors found the Aslamazov-Larkin- (AL-) type VCs for the bare Coulomb interaction $\hat{U}$, which we call the U-VC, induces the orbital order under moderate spin fluctuations [15,17,18]. In Refs. [19,20], this mechanism has been applied to explain the nematic charge-density wave in cuprate superconductors [21,22].

In our previous study for Ba122 systems [10], the U-VC had been neglected. However, the U-VC due to the AL-VC is significant not only for the charge susceptibility, but also for the electron-boson coupling in the gap equation. In fact, the Migdal theorem cannot be applied to strongly correlated superconductors with strong spin/charge fluctuations. In Refs. [23–26], we have shown that the orbital-fluctuation-driven attractive interaction is strongly enlarged by the AL-type U-VC. In Fe-based superconductors, both ferro- and antiferro-orbital fluctuations develop, and the attractive pairing interaction is strongly magnified by the U-VC that is neglected in the Migdal approximation [23,26]. In both La1111 and FeSe, the s_{++}-wave state is naturally obtained by introducing the U-VC into the gap equation by formulating the gap equation going beyond the Migdal-Eliashberg (ME) formalism.

In Ref. [10], we introduced a phenomenological interorbital quadrupole interaction to realize the strong orbital fluctuations in four t_{2g} and z^2 orbitals within the RPA. However, it is highly nontrivial whether strong orbital fluctuations appear in four d orbitals comparably by including the U-VC or not, based on the

Ba122 model with on-site Hubbard interaction. It is a highly nontrivial theoretical challenge to explain the relation $\Delta_{h,z^2} \approx \Delta_{h,t_{2g}}$ based on the realistic Hubbard model for Ba122 systems.

In the present paper, we revisit the study of the pairing mechanism and gap structure in $\mathrm{BaFe_2(As,P)_2}$, which has been discussed for years as one of the central issues in Fe-based superconductors. For this purpose, we construct the effective two-dimensional tight-binding model for $\mathrm{BaFe_2(As,P)_2}$ in which the FSs are composed of four t_{2g} and z^2 orbitals. Based on this model, we analyze the electronic states based on the self-consistent vertex correction (SC-VC) method [15]. Due to the AL-type U-VC, strong ferro-orbital and antiferro-orbital fluctuations emerge in four d orbitals comparably. For this reason, the nearly isotropic gap function appears on all hole FSs, including the z^2-orbital outer hole FS. In contrast, loop nodes are expected to appear on the electron FSs for the wide parameter range. Thus, the present paper satisfactorily explains two characteristics of the gap structure in $\mathrm{BaFe_2(As,P)_2}$: the absence of the horizontal node on hole FSs and the presence of loop nodes on electron FSs.

II. MODEL HAMILTONIAN

In this paper, we introduce the two-dimensional five-orbital model for $\mathrm{BaFe_2(As,P)_2}$ with the $3d$-orbitals z^2, xz, yz, xy, x^2-y^2 on a Fe ion (orbitals 1–5). We derive the present model from the three-dimensional ten-orbital model for the optimally doped $\mathrm{BaFe_2(As,P)_2}$ (30% P doped) introduced in Ref. [10]. Its three-dimensional FSs and Brillouin zone are shown in Fig. 1(a). The black, green, red, and blue colors show the weight of the z^2, xz, yz, and xy orbitals. As shown in Fig. 1(a), both $\boldsymbol{k} = (0,0,\pi)$ and $\boldsymbol{k} = (\pi,\pi,0)$ correspond to the same Z point because $\mathrm{BaFe_2(As,P)_2}$ has a body-centered tetragonal structure. Therefore, we can analyze the gap structure around the Z point based on the two-dimensional model on the $k_z = 0$ plane. The outer hole cylinder around the Z point is composed of the z^2 orbital as shown in Figs. 1(b) and 1(c). Figure 1(c) illustrates a schematic of the hole cylinder on which the weight of the z^2 orbital is shown. The weight of the z^2 orbital is approximately 0.9 around the Z point and almost 0 around the Γ point. The gap structure on this hole cylinder around the Z point is the main topic of this paper.

The FS and band structure of the ten-orbital model on the $k_z = 0$ plane are shown in Fig. 1(d). Two electron FSs around the $X(Y)$ point are composed of the xz, yz, and xy orbitals. Three hole FSs around the Γ point and the inner and middle hole FSs around the Z point are composed of the xz, yz, and xy orbitals. The outer hole FS around the Z point is composed of the z^2 orbital. By unfolding the ten-orbital model according to Refs. [1,27], we derive the two-dimensional five-orbital model with the FSs and band structure shown in Fig. 1(e). The hole FSs ($h1$, $h2$) around the Γ point are composed of the xz and yz orbitals, and the hole FSs ($h3$, $h4$) around the Z point are composed of the xy and z^2 orbitals. The electron FSs ($e1$, $e2$) around the X and Y points are composed of the xz, yz, and xy orbitals. The FS structure of the obtained $\mathrm{BaFe_2(As,P)_2}$ model is essentially equivalent to that of the LaFeAsO model in Ref. [23] with the additional z^2 orbital hole FS ($h4$). We study the mechanism of superconductivity in the optimally doped $\mathrm{BaFe_2(As,P)_2}$ based on the obtained two-dimensional five-orbital Hubbard model,

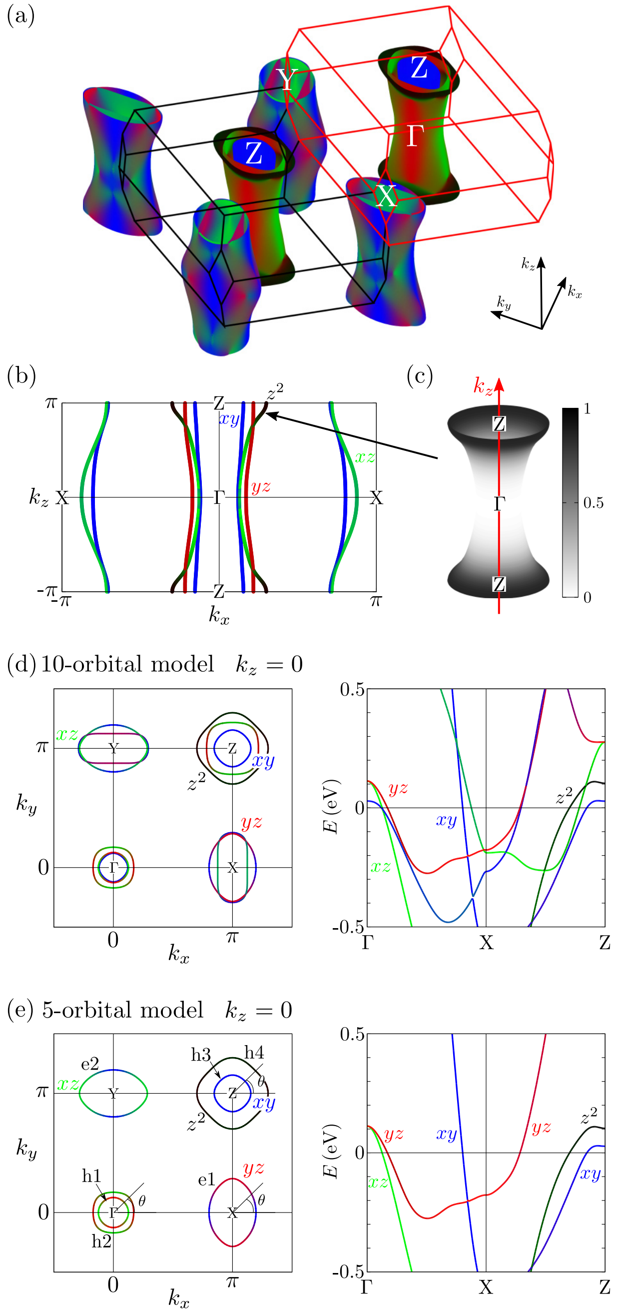

FIG. 1. (a) The three-dimensional FS of the optimally doped $\mathrm{BaFe_2(As,P)_2}$. The solid lines show the Brillouin zone. The black, green (light gray), red (gray), and blue (dark gray) colors show the weight of the z^2, xz, yz, and xy orbitals, respectively. (b) FS on the $k_y = 0$ plane. (c) Schematic of the hole cylinder with the k_z dependence of the weight of the z^2 orbital. (d) The FS and band structure of the ten-orbital model on the $k_z = 0$ plane. Both $\boldsymbol{k} = (0,0,\pi)$ and $\boldsymbol{k} = (\pi,\pi,0)$ are the same Z point. (e) The FS and band dispersions of the two-dimensional five-orbital model derived by unfolding the ten-orbital model in (d). The FS is essentially equal to that of the LaFeAsO model except for the additional $h4$ composed of the z^2 orbital.

$$H = H_0 + H_U. \tag{1}$$

The kinetic term H_0 is expressed as

$$H_0 = \sum_{\boldsymbol{k},\sigma,l,m} H^0_{l,m}(\boldsymbol{k}) c^\dagger_{\boldsymbol{k},l\sigma} c_{\boldsymbol{k},m\sigma}, \qquad (2)$$

where $\boldsymbol{k} = (k_x, k_y)$, $\sigma = \uparrow$ or $\downarrow$ and $l, m = 1$–5. $H^0_{l,m}(\boldsymbol{k})$ is the two-dimensional five-orbital tight-binding model for $\mathrm{BaFe_2(As,P)_2}$ shown in Fig. 1(e), which is given by putting $k_z = 0$ in the original three-dimensional model. H_U is the multiorbital Coulomb interaction for the d orbitals given as

$$H_U = -\frac{1}{2} \sum_{i,ll',mm'} \sum_{\sigma\rho} U^0_{l\sigma,l'\sigma;m\rho,m'\rho} c^\dagger_{i,l\sigma} c_{i,l'\sigma} c^\dagger_{i,m'\rho} c_{i,m\rho}. \qquad (3)$$

Here,

$$U^0_{l\sigma,l'\sigma';m\rho,m'\rho'} = \frac{1}{2} U^{0c}_{l,l';m,m'} \delta_{\sigma,\sigma'} \delta_{\rho',\rho} + \frac{1}{2} U^{0s}_{l,l';m,m'} \boldsymbol{\sigma}_{\sigma,\sigma'} \cdot \boldsymbol{\sigma}_{\rho',\rho}, \qquad (4)$$

where $\boldsymbol{\sigma} = (\sigma_x, \sigma_y, \sigma_z)$ is the Pauli matrix vector. $\hat{U}^{0s}$ and $\hat{U}^{0c}$ are the bare Coulomb interaction matrices for the spin and charge channels, which are composed of the intraorbital Coulomb interaction U, the interorbital one U', Hund's interaction J, and pair transfer J' [17]. Here, we assume the relation $U = U' + 2J$ and $J = J'$.

III. ORBITAL AND SPIN SUSCEPTIBILITIES

Based on the five-orbital Hubbard model for $\mathrm{BaFe_2(As,P)_2}$, we calculate the orbital and spin susceptibilities based on the SC-VC theory [15]. In the SC-VC theory, we consider the AL-VC, which describes orbital-spin interference. Note that any VCs are ignored in the RPA. The irreducible susceptibility including the AL-VC is given in Ref. [26],

$$\hat{\Phi}^{c(s)}(q) = -T \sum_k \hat{G}(k+q)\hat{G}(k)[\hat{1} + \hat{\Lambda}^{\mathrm{AL},c(s)}(k+q,k)], \qquad (5)$$

where $k = (\boldsymbol{k}, \epsilon_n)$ and $q = (\boldsymbol{q}, \omega_l)$; $\epsilon_n = (2n+1)\pi T$ ($\omega_l = 2l\pi T$) is the fermion (boson) Matsubara frequency. $\hat{G}(k) = [(i\epsilon_n + \mu)\hat{1} - \hat{H}_0]^{-1}$ is the Green's function, and μ is the chemical potential. The diagrammatic expression of $\hat{\Phi}^{c(s)}(q)$ is shown in Fig. 2(a). The detailed expression of $\hat{\Lambda}^{\mathrm{AL},c(s)}$ is given in Ref. [26]. The charge (spin) susceptibility is given as

$$\hat{\chi}^{c(s)}(q) = \hat{\Phi}^{c(s)}(q)\{\hat{1} - \hat{U}^{0c(s)}\hat{\Phi}^{c(s)}(q)\}^{-1}. \qquad (6)$$

The charge (spin) susceptibility diverges when the charge (spin) Stoner factor $\alpha_{c(s)}$, which is given by the maximum eigenvalue of $\hat{U}^{0c(s)}\hat{\Phi}^{c(s)}(\boldsymbol{q}, 0)$, reaches unity. In the RPA analysis ($\hat{\Lambda}^{\mathrm{AL},c(s)} = 0$), the relation $\alpha_s > \alpha_c$ always holds for $J > 0$, and $\chi^c(q)$ remains small even when $\chi^s(q)$ develops divergently. In contrast, the spin-fluctuation-driven orbital order or fluctuations are realized when we consider the VC since the AL-VC increases in proportion to $\sum_p \chi^s(q+p)\chi^s(p)$ near the magnetic quantum critical point [15]. We neglect the spin-channel AL-VC and Maki-Thompson VC (MT-VC) for susceptibilities since they are negligible in various models. Figure 2(b) shows the linearized gap equation with the U-VC.

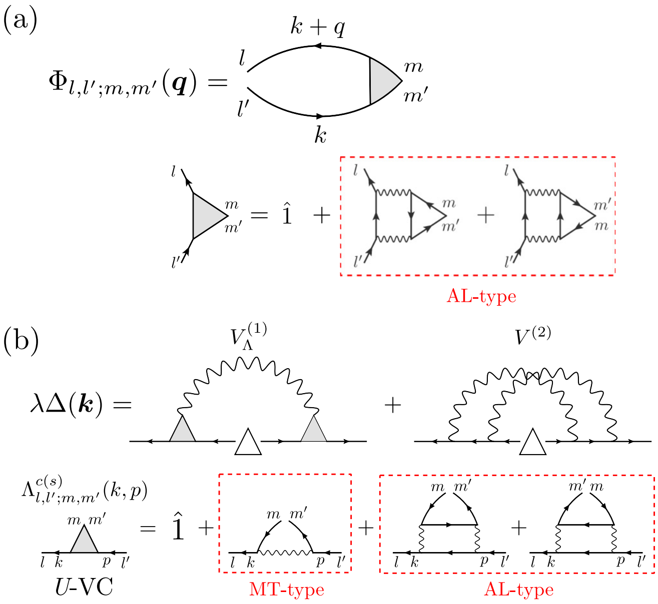

FIG. 2. (a) The irreducible susceptibility including the AL-VC. (b) The superconducting gap equation in the present theory. The U-VC composed of the MT- and AL-type VCs enhances (suppresses) the attractive (repulsive) term. The $V^{(2)}$ term induces the attractive interaction in the present multiorbital model.

Hereafter, we carry out the calculation with 32×32 $\boldsymbol{k}$ mesh and 256 Matsubara frequencies. We fix the temperature at $T = 20$ meV and the ratio $J/U = 0.1$. Figures 3(a) and 3(b) are the spin and nematic orbital susceptibilities for $U = 1.4$ eV. The obtained spin and charge Stoner factors are $(\alpha_s, \alpha_c) = (0.97, 0.88)$. The spin susceptibility $\chi^s(\boldsymbol{q}) = \sum_{l,m} \chi^s_{l,l;m,m}(\boldsymbol{q})$ shows the maximum peak at $\boldsymbol{q} \simeq (\pi, 0)$ due to the FS nesting, consistently with the magnetic order in underdoped compounds [28–30]. The nematic susceptibility $\chi^{\mathrm{nem}}(\boldsymbol{q}) = \chi^c_{2,2;2,2}(\boldsymbol{q}) + \chi^c_{3,3;3,3}(\boldsymbol{q}) - \chi^c_{2,2;3,3}(\boldsymbol{q}) - \chi^c_{3,3;2,2}(\boldsymbol{q})$ shows the maximum peak at $\boldsymbol{q} = (0, 0)$. The development of the nematic fluctuations is experimentally observed near the orthorhombic phase [31–34]. We also show the nematic orbital susceptibility given by the RPA in Fig. 3(b). Since it remains small, the structural phase transition cannot be explained by the RPA.

Figure 4 shows the intraorbital spin susceptibilities $\chi^s_{l,l;l,l}(\boldsymbol{q})$ for (a) $l = 1$, (b) $l = 3$, and (c) $l = 4$. $\chi^s_{1,1;1,1}(\boldsymbol{q})$ shows the broad peak around $\boldsymbol{q} \sim \boldsymbol{0}$ due to the intra-FS nesting in $h4$. There is no inter-FS nesting because of the absence of the z^2-orbital weight in other FSs. $\chi^s_{2,2;2,2}(\boldsymbol{q})$ and $\chi^s_{3,3;3,3}(\boldsymbol{q})$ are strongly enlarged due to nesting between $h1$, $h2$ and $e1$, $e2$. Thus, spin fluctuations develop most strongly on the xz and yz orbitals. [Note that $\chi^{s(c)}_{2,2;2,2}(q_x, q_y) = \chi^{s(c)}_{3,3;3,3}(q_y, q_x)$.] $\chi^s_{4,4;4,4}(\boldsymbol{q})$ is also enlarged due to the nesting between $h3$ and $e1$, $e2$.

Figure 5 shows the intraorbital charge susceptibilities $\chi^c_{l,l;l,l}(\boldsymbol{q})$ for (a) $l = 1$, (b) $l = 3$, and (c) $l = 4$. $\chi^c_{1,1;1,1}(\boldsymbol{q})$ shows the broad peak around $\boldsymbol{q} = (0, 0)$, and $\chi^c_{3,3;3,3}(\boldsymbol{q})$, $\chi^c_{4,4;4,4}(\boldsymbol{q})$ show large ferro- and antiferrofluctuations. The interorbital charge susceptibilities $\chi^c_{1,2;1,2}(\boldsymbol{q})$ and $\chi^c_{1,4;1,4}(\boldsymbol{q})$ are also shown in Figs. 5(d) and 5(e). These large charge fluctuations are caused by the AL-VC for the charge channel.

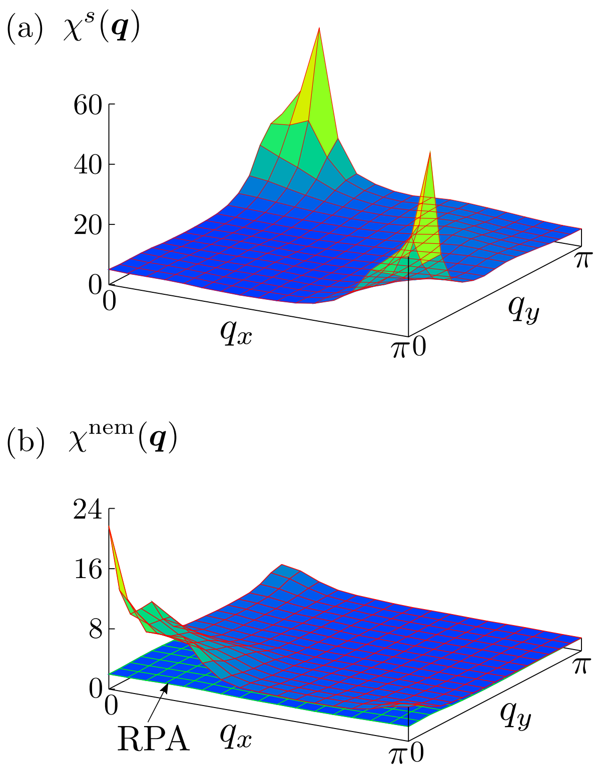

FIG. 3. (a) The spin susceptibility $\chi^s(\boldsymbol{q}) = \sum_{l,m}\chi^s_{l,l;m,m}(\boldsymbol{q})$. (b) The nematic orbital susceptibility $\chi^{\mathrm{nem}}(\boldsymbol{q}) = \chi^c_{2,2;2,2}(\boldsymbol{q}) + \chi^c_{3,3;3,3}(\boldsymbol{q}) - \chi^c_{2,2;3,3}(\boldsymbol{q}) - \chi^c_{3,3;2,2}(\boldsymbol{q})$ obtained by the SC-VC method. We also show $\chi^{\mathrm{nem}}(\boldsymbol{q})$ obtained by the RPA.

IV. GAP EQUATION BEYOND THE MIGDAL-ELIASHBERG FORMALISM

In this section, we solve the linearized gap equation depicted in Fig. 2(b), concentrating on the superconducting gap function on the FSs [10].

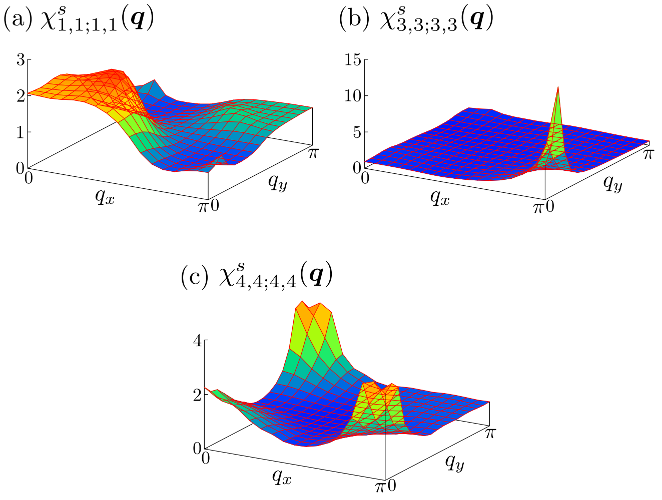

FIG. 4. The spin susceptibilities $\chi^s_{l,l;l,l}(\boldsymbol{q})$ for (a) $l = 1$, (b) $l = 3$, and (c) $l = 4$. $\chi^s_{1,1;1,1}(\boldsymbol{q})$ moderately develops due to intra-FS nesting. $\chi^s_{3,3;3,3}(\boldsymbol{q})$ and $\chi^s_{4,4;4,4}(\boldsymbol{q})$ show large peaks at the inter-FS nesting vectors.

The equation is expressed as

$$\begin{aligned}Z_\alpha(\boldsymbol{k},\epsilon_n)\lambda\Delta_\alpha(\boldsymbol{k},\epsilon_n) &= -\frac{\pi T}{(2\pi)^2}\sum_{\beta,m}\oint_{\mathrm{FS}_\beta}\frac{d\boldsymbol{p}}{v^\beta(\boldsymbol{p})}\{V^{\mathrm{pair}}_{\alpha,\beta}(\boldsymbol{k},\epsilon_n,\boldsymbol{p},\epsilon_m)\\ &\quad + V^{\mathrm{imp}}_{\alpha,\beta}(\boldsymbol{k},\boldsymbol{p};\epsilon_n)\delta_{n,m}\}\frac{\Delta_\beta(\boldsymbol{p},\epsilon_m)}{|\epsilon_m|},\end{aligned} \tag{7}$$

where $\Delta_\alpha(k)$ is the superconducting gap function and α,β are indices of the FS. The eigenvalue λ is approximately proportional to T_c, and $\lambda = 1$ is satisfied at $T = T_c$. $V^{\mathrm{pair}}_{\alpha,\beta}(k,p)$ is the pairing interaction in the band-diagonal basis given as

$$\begin{aligned}V^{\mathrm{pair}}_{\alpha,\beta}(k,p) &= \sum_{ll'mm'}V^{\mathrm{pair}}_{l,l';m,m'}(k,p)\\ &\quad\times u^*_{l\alpha}(\boldsymbol{k})u_{l'\beta}(\boldsymbol{p})u_{m\beta}(-\boldsymbol{p})u^*_{m'\alpha}(-\boldsymbol{k}),\end{aligned} \tag{8}$$

where $u_{l\alpha}(\boldsymbol{k}) = \langle l|\boldsymbol{k};\alpha\rangle$ is the unitary matrix that connects between the band basis and the orbital basis. [The expression of $V^{\mathrm{pair}}(k,p)$ will be presented at the end of this section; see Eq. (23).] We consider the impurity effect based on the T-matrix approximation. $V^{\mathrm{imp}}(\boldsymbol{k},\boldsymbol{p};\epsilon_n)$, which is induced by impurities, is given as

$$\begin{aligned}V^{\mathrm{imp}}_{\alpha,\beta}(\boldsymbol{k},\boldsymbol{p};\epsilon_n) &= -\frac{n_{\mathrm{imp}}}{T}\sum_{ll'mm'}T_{ll'}(\epsilon_n)T_{mm'}(-\epsilon_n)\\ &\quad\times u^*_{l\alpha}(\boldsymbol{k})u_{l'\beta}(\boldsymbol{p})u_{m\beta}(-\boldsymbol{p})u^*_{m'\alpha}(-\boldsymbol{k}),\end{aligned} \tag{9}$$

where n_{imp} is the impurity concentration. We consider the diagonal impurity potential I_{imp} in the d-orbital basis. The T matrix for an impurity is given as

$$\hat{T}(\epsilon_n) = [\hat{1} - \hat{I}\hat{G}_{\mathrm{loc}}(\epsilon_n)]^{-1}\hat{I}. \tag{10}$$

Here, $I_{ll'} = I_{\mathrm{imp}}\delta_{l,l'}$, and $[G_{\mathrm{loc}}(\epsilon_n)]_{ll'} = \sum_{\boldsymbol{k}} G_{ll'}(\boldsymbol{k},\epsilon_n)$ is the local Green's function. The normal self-energy induced by impurities is given as

$$\delta\sigma^n_\alpha(\boldsymbol{k},\epsilon_n) = n_{\mathrm{imp}}\sum_{ll'}u^*_{l\alpha}(\boldsymbol{k})T_{ll'}(\epsilon_n)u_{l'\alpha}(\boldsymbol{k}). \tag{11}$$

Then, $Z_\alpha(\boldsymbol{k},\epsilon_n)$ is given as

$$Z_\alpha(\boldsymbol{k},\epsilon_n) = 1 + \frac{\gamma^\alpha(\boldsymbol{k},\epsilon_n)}{|\epsilon_n|}, \tag{12}$$

where $\gamma^\alpha(\boldsymbol{k},\epsilon_n) = -\mathrm{Im}\,\delta\sigma^n_\alpha(\boldsymbol{k},\epsilon_n)\mathrm{sgn}(\epsilon_n)$ is the impurity-induced quasiparticle damping rate.

Beyond the ME formalism, we take the U-VC for the coupling constant into account. The MT-VC and AL-VC for the U-VC are depicted in Fig. 2(b), and their analytic expressions are given in Ref. [26]. The total U-VC for the charge (spin) channel is

$$\hat{\Lambda}^{c(s)}(k,k') = \hat{1} + \hat{\Lambda}^{\mathrm{MT},c(s)}(k,k') + \hat{\Lambda}^{\mathrm{AL},c(s)}(k,k'). \tag{13}$$

The effect of the spin-channel AL-VC on $\hat{\chi}^s(\boldsymbol{q})$ is small since $|\Lambda^{\mathrm{AL},s(c)}(k+q,k)| \ll 1$ except for low Matsubara frequencies [26]. In contrast, the AL-VC in the gap equation is important since Cooper pairs are formed by low-energy quasiparticles. By taking the U-VC into account, the

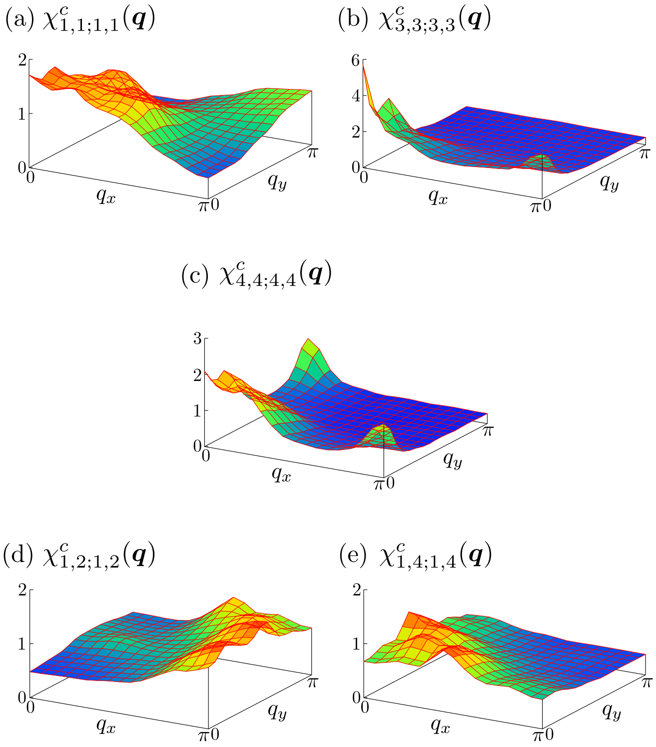

FIG. 5. The intraorbital charge susceptibilities $\chi^c_{l,l;l,l}(\boldsymbol{q})$ for (a) $l=1$, (b) $l=3$, and (c) $l=4$. $\chi^c_{1,1;1,1}(\boldsymbol{q})$ shows the broad peak around $\boldsymbol{q}=(0,0)$. $\chi^c_{3,3;3,3}(\boldsymbol{q})$ and $\chi^c_{4,4;4,4}(\boldsymbol{q})$ exhibit both the ferro- and the antiferropeaks. The interorbital charge susceptibilities are (d) $\chi^c_{1,2;1,2}(\boldsymbol{q})$ and (c) $\chi^c_{1,4;1,4}(\boldsymbol{q})$. These charge fluctuations are enlarged by the AL-VC.

single-fluctuation exchange term in the pairing interaction is given as

$$\hat{V}^{(1)}_{\Lambda}(k,p)=\hat{V}^{(1)s}_{\Lambda}(k,p)+\hat{V}^{(1)c}_{\Lambda}(k,p)+\hat{V}^{0}, \tag{14}$$

where

$$\hat{V}^{(1)s}_{\Lambda}(k,p)=\tfrac{3}{2}\hat{V}^{\Lambda,s}(k,p), \tag{15}$$

$$\hat{V}^{(1)c}_{\Lambda}(k,p)=-\tfrac{1}{2}\hat{V}^{\Lambda,c}(k,p), \tag{16}$$

$$\hat{V}^{0}=-\hat{U}^{0s}. \tag{17}$$

Equations (15) and (16) represent the spin- and charge-fluctuation-mediated interaction terms with U-VCs, and Eq. (17) is necessary to eliminate the double-counting. Here, $\hat{V}^{\Lambda,c(s)}$ is given as

$$\hat{V}^{\Lambda c(s)}(k,p)=\hat{\Lambda}^{c(s)}(k,p)\hat{V}^{c(s)}(k-p)\hat{\bar{\Lambda}}^{c(s)}(-k,-p), \tag{18}$$

where

$$\hat{V}^{c(s)}(k-p)=\hat{U}^{0c(s)}+\hat{U}^{0c(s)}\hat{\chi}^{c(s)}(k-p)\hat{U}^{0c(s)}, \tag{19}$$

$$\hat{\bar{\Lambda}}^{c(s)}_{l,l';m,m'}(k,p)=\hat{\Lambda}^{c(s)}_{m,m';l,l'}(k,p). \tag{20}$$

The pairing interaction due to the charge (spin) fluctuations is enhanced (suppressed) by the U-VC since $|\Lambda^{c(s)}(k,p)|^2$ is larger (smaller) than 1.

To discuss the importance of the U-VC, we also study the pairing interaction given by the RPA without U-VC ($\hat{\Lambda}^{c,s}=\hat{1}$) in later sections,

$$\hat{V}^{(1)}_{\rm RPA}(k-p)=\hat{V}^{(1)s}_{\rm RPA}(k-p)+\hat{V}^{(1)c}_{\rm RPA}(k-p)+\hat{V}^{0}. \tag{21}$$

In this ME formalism, $\hat{V}^{(1)s}_{\rm RPA}$ is important because only spin fluctuations develop in the RPA.

In addition, we calculate the double-fluctuation exchange pairing interaction $V^{(2)}$ term, which corresponds to the AL process for the pairing interaction. It is given as

$$\begin{aligned}V^{(2)}_{l,l';m,m'}(k,p)=\frac{T}{4}\sum_{q}\sum_{a,b,c,d}&G_{a,b}(p-q)G_{c,d}(-k-q)\\&\times\{3V^{s}_{l,a,m,d}(k-p+q)V^{s}_{b,l',c,m'}(-q)\\&+3V^{s}_{l,a,m,d}(k-p+q)V^{c}_{b,l',c,m'}(-q)\\&+3V^{c}_{l,a,m,d}(k-p+q)V^{s}_{b,l',c,m'}(-q)\\&-V^{c}_{l,a,m,d}(k-p+q)V^{c}_{b,l',c,m'}(-q)\}.\end{aligned} \tag{22}$$

In the present model, $V^{(2)}$ induces an attractive [repulsive] interaction for $\boldsymbol{k}-\boldsymbol{p}\approx(\pi,0)$ [$\boldsymbol{k}-\boldsymbol{p}\approx(0,0)$] as we discussed in Ref. [26] in detail. The total pairing interaction in the present beyond-ME formalism is given as

$$\hat{V}^{\rm total}_{\Lambda}(k,p)=\hat{V}^{(1)}_{\Lambda}(k,p)+\hat{V}^{(2)}(k,p). \tag{23}$$

V. THE s_{++}-WAVE STATE WITHOUT A HORIZONTAL NODE

Hereafter, we discuss the obtained gap functions at $\alpha_s=0.97$ and $J/U=0.1$. Figure 6(a) is the gap function derived from $\hat{V}^{(1)}_{\rm RPA}$, which is the pairing interaction in the ME formalism. This is the fully gapped s_{+-}-wave state with very small $|\Delta_{h4}|$: The sign reversal between $h4$ and $h1$ corresponds to the presence of the horizontal node, which is expressed by the schematic gap structure in Fig. 6(b). The broken lines represent the expected horizontal node. This result is consistent with the previous RPA results in Ref. [6]. However, both the ARPES studies in Refs. [7,8] and the small Volovik effect in the specific-heat measurement in Refs. [35,36] indicate the absence of a horizontal node.

Figure 6(c) is the gap function derived from $\hat{V}^{\rm total}$. In this case, the nodal s-wave state is obtained. There is no sign reversal between $h4$ and $h1$, that corresponds to the absence of the horizontal node expressed by the schematic gap structure in Fig. 6(d). This result is consistent with the ARPES studies in Refs. [7,8]. We call it the nodal s_{+-}-wave state since the gap on $e1$ is mainly negative, that is, $\langle\Delta_{e1}(k)\rangle_{\rm FS}<0$. When we neglect the U-VC in the gap equation, we obtain the s_{+-}-wave state essentially similar to the gap structure in Fig. 6(a). This fact means that the U-VC must be included in the gap equation to obtain reliable results.

In Fig. 6(c), nodes appear only on the electron FSs at which the orbital character gradually changes between $xz(yz)$ and xy. This result means the emergence of the loop nodes on

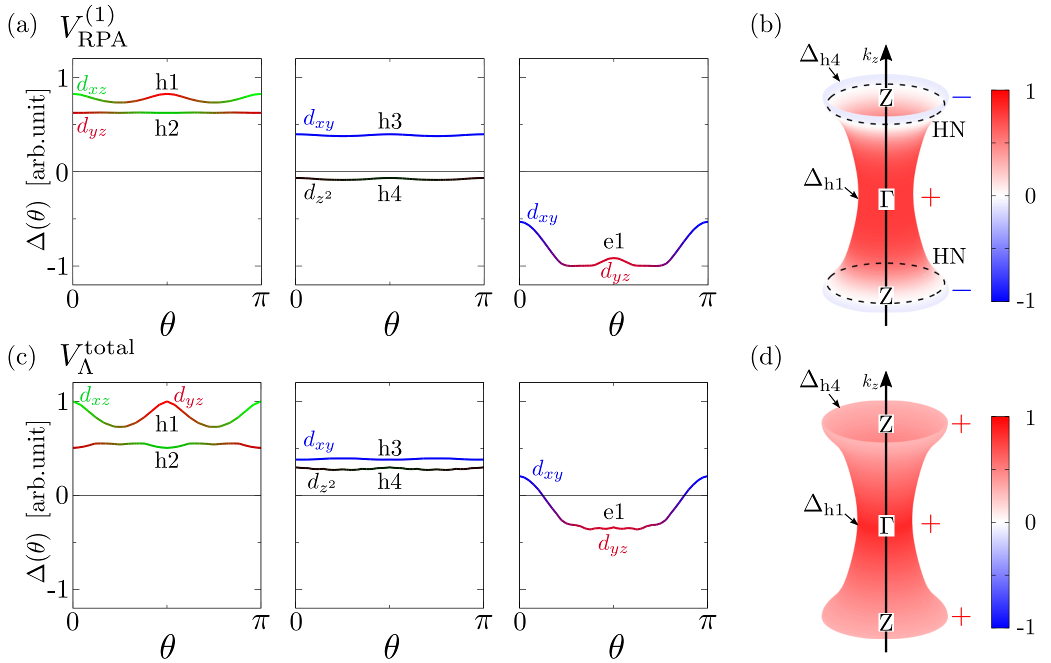

FIG. 6. (a) The fully gapped s_{+-}-wave state given by $V^{(1)}_{\rm RPA}$. There is sign reversal between $h4$ and $h1$, that corresponds to the schematic horizontal node gap structure in (b). The broken lines represent the expected horizontal node (HN). (c) The nodal s-wave state given by $V^{\rm total}_{\Lambda}$ (nearly s_{+-}). There is no sign reversal between $h4$ and $h1$, which corresponds to the schematic gap structure without a horizontal node in (d).

the electron FSs, consistent with the theoretical prediction in Ref. [10] and the angle-resolved thermal conductivity measurement [37].

A. The J/U and impurity dependences of the gap structure

As shown in Fig. 6(c), we obtained the nodal s-wave state with a large gap on $h4$ by applying the present beyond-ME formalism. Here, we discuss impurity effect on the gap structure. We consider the on-site intraorbital impurity potential with $I_{\rm imp} = 1$ eV. Figure 7(a) shows the obtained gap function for $\alpha_s = 0.97$ and $J/U = 0.1$ in the presence of the 3% impurities ($n_{\rm imp} = 0.03$). The gap on $e1$ is mainly positive $[\langle\Delta_{e1}(k)\rangle_{\rm FS} > 0]$, so we call it the nodal s_{++}-wave state. With increasing $n_{\rm imp}$, we obtain the fully gapped s_{++}-wave state as shown in Fig. 7(b) for $n_{\rm imp} = 0.05$. Thus, impurity-induced $s_{+-} \rightarrow s_{++}$ crossover is realized in the present paper [5,38].

The gap structure sensitively depends on the Stoner factor and model parameters. In Fig. 7(c), we show the gap structure obtained for $\alpha_s = 0.94$ and $n_{\rm imp} = 0.05$. The obtained fully gapped s_{++}-wave function becomes more isotropic compared with the gap in Fig. 7(b).

Next, we show the α_s-J/U phase diagrams of the gap structure in Fig. 8 in the case of (a) $n_{\rm imp} = 0$, (b) $n_{\rm imp} = 0.03$, and (c) $n_{\rm imp} = 0.05$. The red circles, yellow upper triangles, green lower triangles, and blue squares represent the fully gapped s_{++}-wave, the nodal s_{++}-wave $[\langle\Delta_{e1}(k)\rangle_{\rm FS} > 0]$, the nodal s_{+-}-wave $[\langle\Delta_{e1}(k)\rangle_{\rm FS} < 0]$, and the fully gapped s_{+-}-wave states, respectively. In Fig. 8(a), both s_{++}-wave and s_{+-}-wave states appear. In contrast, in Fig. 8(b), the s_{++}-wave state is realized in the wide parameter range. The range of the s_{++}-wave state is expanded further by increasing the impurity concentration as shown in Fig. 8(c). The phase diagrams (a)–(c) show that the crossover between the s_{+-}-wave state and the s_{++}-wave state is caused by a small amount of impurities.

To discuss the impurity effect on $T_{\rm c}$, we show the impurity dependence of the normalized eigenvalue λ/λ_0, where λ_0 is the eigenvalue at $n_{\rm imp} = 0$. Figures 8(d) and 8(e) show the obtained λ/λ_0 given by the RPA and the present theory, respectively. $\lambda_0 = 1.4$ in the RPA analysis, and $\lambda_0 = 1.2$ in the present theory. In the RPA, λ/λ_0 decreases drastically, which indicates the drastic reduction in $T_{\rm c}$. In contrast, the decrease in λ/λ_0 given by the present theory is small, which indicates the small reduction in $T_{\rm c}$ during the $s_{+-} \rightarrow s_{++}$ crossover [5,38]. In fact, the robustness of $T_{\rm c}$ against impurities is confirmed in many Fe-based superconductors [39–42]. We expect that the s_{++}-wave state is realized in real compounds due to small amount of impurities.

B. The mechanism of the s_{++}-wave state with the absence of a horizontal node on the FS composed of the z^2 orbital

Here, we explain the reason why the s_{++}-wave state is obtained in the present paper. To clarify the pairing interaction between FSs, we define the averaged pairing interaction between α and β as

$$\bar{V}(\alpha,\beta) = \frac{\oint d\boldsymbol{k}_\alpha d\boldsymbol{k}_\beta V^{\rm pair}_{\alpha,\beta}(\boldsymbol{k}_\alpha,\boldsymbol{k}_\beta)}{\oint d\boldsymbol{k}_\alpha d\boldsymbol{k}_\beta}, \qquad (24)$$

where $\boldsymbol{k}_\alpha$ is the Fermi wave number on the FS denoted by α. We show $\bar{V}(\alpha,\beta)$ in Figs. 9(a) $V^{\rm pair}_{\alpha,\beta} = V^{(1)s}_{\rm RPA}$, 9(b) $V^{(1)c}_{\rm RPA}$, 9(c) $V^{(1)s}_{\Lambda}$, 9(d) $V^{(1)c}_{\Lambda}$, and 9(e) $V^{(2)}$. The blue and red panels mean that interaction between FSs is attractive and repulsive, respectively. In the RPA analysis, the repulsive interaction by

(a) nodal s_{++} ($\alpha_s = 0.97, J/U = 0.1, n_{\rm imp} = 0.03$)

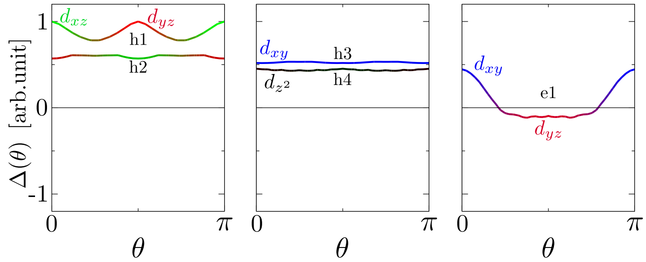

(b) fully gapped s_{++} ($\alpha_s = 0.97, J/U = 0.1, n_{\rm imp} = 0.05$)

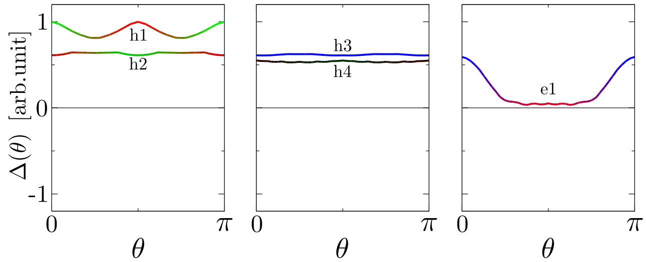

(c) fully gapped s_{++} ($\alpha_s = 0.94, J/U = 0.1, n_{\rm imp} = 0.05$)

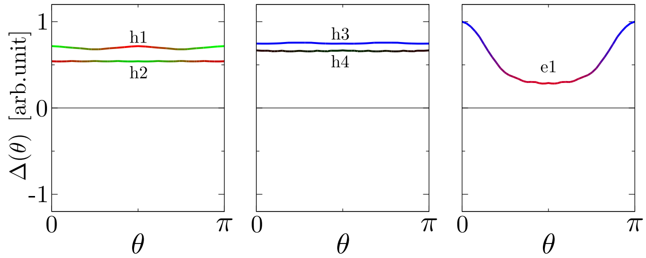

FIG. 7. The θ dependence of the gap structure. (a) The nodal s-wave state at $\alpha_s = 0.97$, $J/U = 0.1$, and $n_{\rm imp} = 0.03$ (nearly s_{++}). (b) The fully gapped s_{++}-wave state at $\alpha_s = 0.97$, $J/U = 0.1$, and $n_{\rm imp} = 0.05$. (c) The perfectly fully gapped s_{++}-wave state at $\alpha_s = 0.94$, $J/U = 0.1$, and $n_{\rm imp} = 0.05$.

$V_{\rm RPA}^{(1)s}$ is dominant. The repulsive interaction is strong between $h1$–$h3$ and $e1$. The repulsive interaction is given by intraorbital spin fluctuations ($\chi^s_{2,2;2,2}$, $\chi^s_{3,3;3,3}$, and $\chi^s_{4,4;4,4}$) and induces the s_{+-}-wave state. In contrast, the inter-FS repulsive interaction between $h4$ and the other FSs is weak as shown in panels $(h4, \beta)$ for $\beta \neq h4$ in Fig. 9(a). A small negative gap in $h4$ is induced by weak repulsive interactions due to interorbital spin fluctuations ($\chi^s_{1,2;2,1}$, $\chi^s_{1,3;3,1}$, and $\chi^s_{1,4;4,1}$).

In high contrast, $\bar{V}_\Lambda^{(1)c}$ shown in Fig. 9(d) is strongly attractive because of the large charge-channel U-VC: $|\Lambda^c_{l,l;l,l}|^2 \gg 1$. Especially, strong attractive interaction in the panels $(h1, h1)$, $(h1, h2)$, and $(h2, h2)$ originates from the ferro-orbital fluctuations at $\boldsymbol{q} = (0, 0)$ shown in Fig. 3(a). Thus, nematic fluctuations are significant for the pairing mechanism. $\bar{V}_\Lambda^{(1)s}$ with the U-VC for the spin channel shown in Fig. 9(c) gives a weak repulsive interaction compared with $\bar{V}_{\rm RPA}^{(1)s}$ because spin-fluctuation-mediated pairing interactions are reduced by $|\Lambda^s_{l,l;l,l}|^2 < 1$. Interestingly, $\bar{V}_\Lambda^{(1)s}(\alpha, \beta)$ for $(\alpha, \beta) = (h1, h3)$, $(h2, h3)$, and $(h3, h4)$ is weakly attractive if the U-VC is taken into account. The reason is shortly explained in the Appendix. Therefore, U-VCs for both spin and charge channels play an important role for realizing the s_{++}-wave state, whereas the s_{+-}-wave state is suppressed. Moreover, $V^{(2)}$ gives an important contribution to the s_{++}-wave state. In fact, both $\bar{V}^{(2)}(e1, h1\text{–}h4)$ and $\bar{V}^{(2)}(h4, h1\text{–}h2)$ give attractive interactions between different FSs. In contrast, $\bar{V}^{(2)}$ gives an intra-FS repulsive interaction. Note that $|V^{(2)}|$ is large when FSs have large xy orbital components, such as $\bar{V}^{(2)}(e1, h3)$.

$\bar{V}_\Lambda^{\rm total}$ without impurity is shown in Fig. 10(a). This total pairing interaction gives the nodal s-wave state shown in Fig. 6(c). The inter-FS and intra-FS interactions in Fig. 10(a), which are attractive or repulsive depending on FSs, are averaged by introducing impurities. For this reason the number of red panels in Fig. 10(b) for $n_{\rm imp} = 0.05$, which shows $\bar{V}_\Lambda^{\rm total} + \bar{V}^{\rm imp}$, is

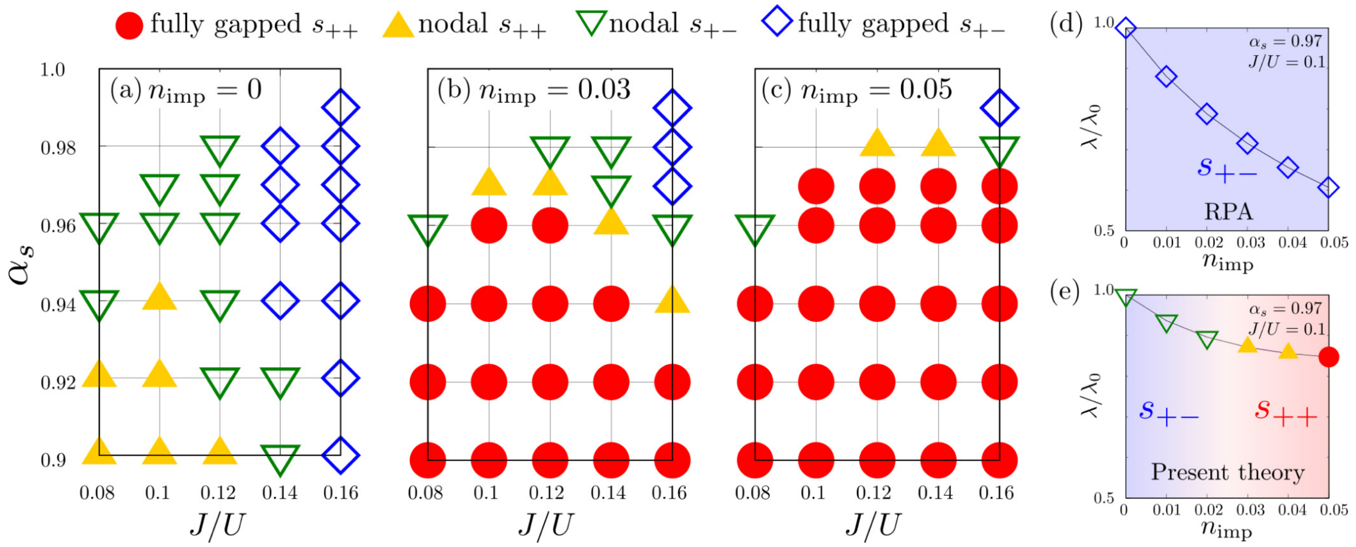

FIG. 8. (a) The α_s-J/U phase diagrams of the gap structure for (a) without impurity, (b) in the presence of the 3% impurity, and (c) in the presence of the 5% impurity, respectively. The red circles, yellow upper triangles, green lower triangles, and blue squares show the fully gapped s_{++}-wave state, the nodal s_{++}-wave state [$\langle \Delta_{e1}(k) \rangle_{\rm FS} > 0$], the nodal s_{+-}-wave state [$\langle \Delta_{e1}(k) \rangle_{\rm FS} < 0$], and the fully gapped s_{+-}-wave state, respectively. The impurity dependence of λ/λ_0 for (d) RPA and (e) the present theory with U-VC.

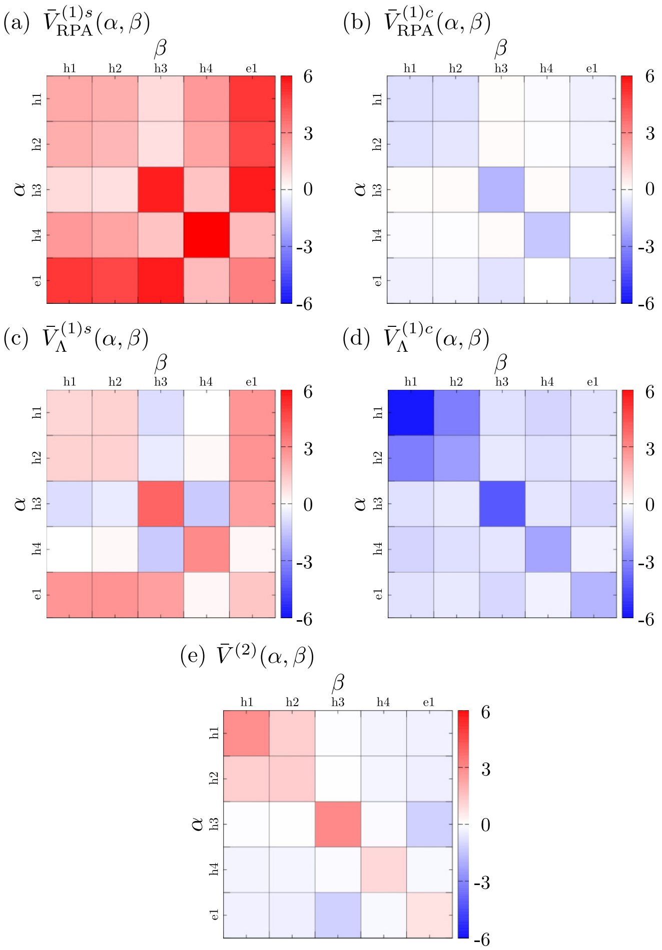

FIG. 9. The averaged pairing interaction between FS_α and FS_β for (a) $V^{(1)s}_{\rm RPA}$, (b) $V^{(1)c}_{\rm RPA}$, (c) $V^{(1)s}_{\Lambda}$, (d) $V^{(1)c}_{\Lambda}$, and (e) $V^{(2)}$. The blue and red panels show that interaction between FSs is attractive and repulsive, respectively. Here, we drop the bare Coulomb repulsive term, which is reduced by the retardation effect.

smaller than that in Fig. 10(a). The pairing interaction at $n_{\rm imp}=0.05$ in Fig. 10(b) gives the fully gapped s_{++}-wave state in Fig. 7(b). Therefore, by introducing a small amount of impurities, the attractive interaction becomes dominant, and therefore, the s_{++}-wave state is realized.

Next, we focus on the gap function in $h4$: We explain the reason why Δ_{h4} is large and $\Delta_{h4}\Delta_{h1}>0$ is realized as shown in Fig. 6(c): This result means that the horizontal node is absent. In Figs. 10(a) and 10(b), we find that $\bar{V}^{\rm total}$ is attractive between $h4$ and the other hole FSs. The attractive interaction between $h4$ and $h1$–$h3$ is given by interorbital fluctuations $\chi^c_{1,m;m,1}$ and $\chi^c_{1,m;1,m}$ $(m=2\text{–}4)$, and they are strongly enlarged by the interorbital U-VC.

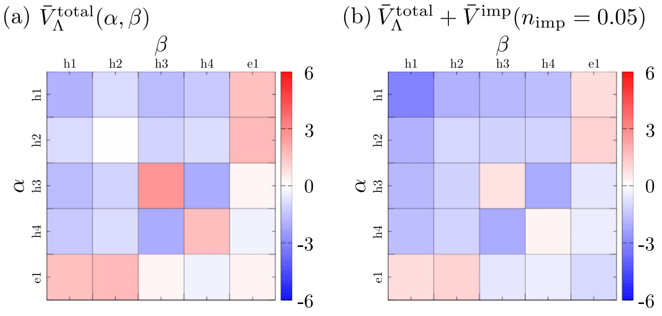

FIG. 10. The averaged $V^{\rm total}$ between FS_α and FS_β for (a) without impurity and (b) in the presence of the 5% impurities.

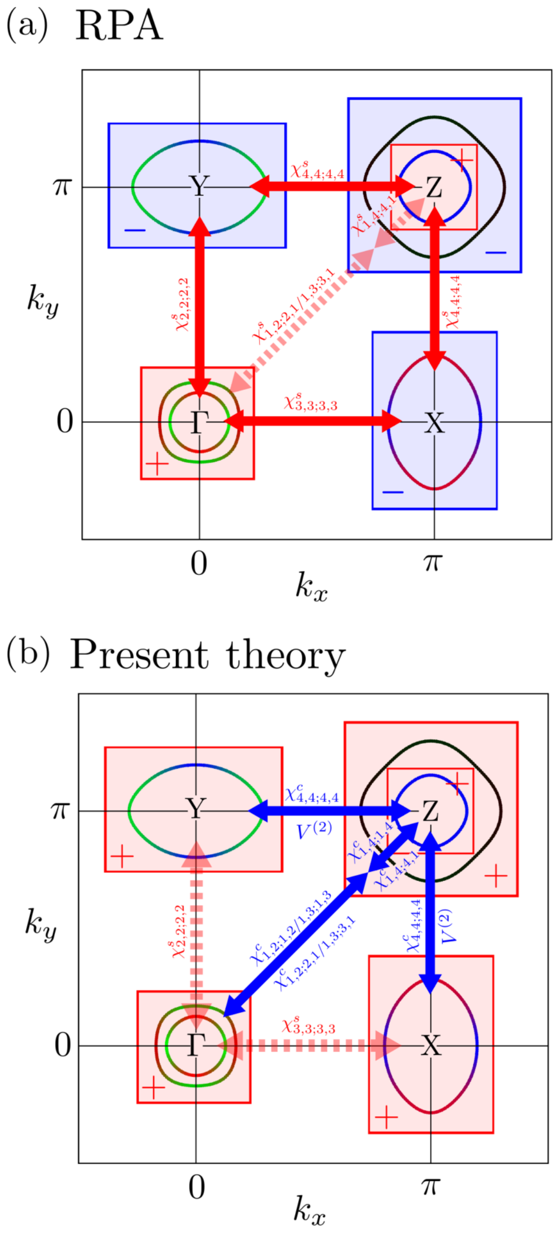

FIG. 11. The schematic pairing interaction between FSs: (a) in the RPA analysis and (b) in the present theory. The blue and red arrows represent attractive and repulsive interactions, respectively. The broken arrows show weak interaction.

We summarize the schematic pairing interactions between FSs given by RPA in Fig. 11(a) and those given by the present theory with U-VCs in Fig. 11(b). In the RPA, strong repulsive interactions driven by intraorbital spin fluctuations are dominant, and the s_{+-}-wave state is realized. The horizontal node appears due to weak repulsive interactions given by interorbital spin fluctuations [6]. In the present

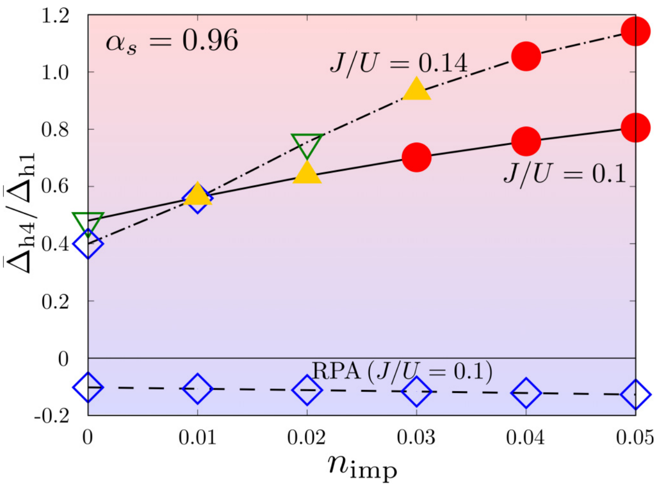

FIG. 12. The impurity dependence of the averaged gap size ratio $\bar{\Delta}_{h4}/\bar{\Delta}_{h1}$ for $\alpha_s = 0.96$. $\bar{\Delta}_{h4}/\bar{\Delta}_{h1} > 0$ indicates the absence of a horizontal node. $\bar{\Delta}_{h4}/\bar{\Delta}_{h1} < 0$ indicates the presence of a horizontal node.

theory with U-VCs, the s_{++}-wave state is realized because the attractive interactions by orbital fluctuations are strongly enhanced whereas repulsive interactions by spin fluctuations are reduced by the U-VCs. $V^{(2)}$ also induces attractive interpocket interaction. In addition, Δ_{h4} is large, and the relation $\Delta_{h1} \simeq \Delta_{h2} \simeq \Delta_{h3} \simeq \Delta_{h4}$ holds due to the interorbital fluctuations as discussed in Ref. [10]. Therefore, the horizontal node is absent in the present beyond-ME theory.

C. Anisotropy of the gap structure

In the previous subsection, we explained that the horizontal node is absent ($\bar{\Delta}_{h4}\bar{\Delta}_{h1} > 0$) due to interorbital attractive interaction. Here, we verify that this feature is very robust for a wide parameter range. Figure 12 is the impurity dependence of the averaged gap size ratio $\bar{\Delta}_{h4}/\bar{\Delta}_{h1}$ where the averaged gap size $\bar{\Delta}_\alpha$ is given as

$$\bar{\Delta}_\alpha = \frac{\oint d\boldsymbol{k}_\alpha \Delta_\alpha(\boldsymbol{k}_\alpha)}{\oint d\boldsymbol{k}_\alpha}. \tag{25}$$

We discuss the results only for $\alpha_s = 0.96$ since the results are almost independent of α_s. In the RPA analysis at $J/U = 0.1$, we obtain $\bar{\Delta}_{h4}/\bar{\Delta}_{h1} \simeq -0.1$ in the whole range of $n_{\rm imp}$. The result is almost independent of J/U. It indicates that the horizontal node is robust in the RPA even if the impurity effect is considered. In contrast, we obtain $\bar{\Delta}_{h4}/\bar{\Delta}_{h1} > 0$ in the present theory with U-VCs, which means that the horizontal node is absent. We find that the ratio $\bar{\Delta}_{h4}/\bar{\Delta}_{h1}$ becomes large with increasing $n_{\rm imp}$ from 0.5 ($n_{\rm imp} = 0$) to 0.8 ($n_{\rm imp} = 0.05$) at $J/U = 0.1$. The horizontal node is absent even for $J/U = 0.14$. We stress that the horizontal node is absent even in the s_{+-}-wave state in the present theory. The ratio $\bar{\Delta}_{h4}/\bar{\Delta}_{h1}$ is predicted to increase with $n_{\rm imp}$.

VI. SUMMARY

In this paper, we studied the superconducting gap structure of BaFe$_2$(As, P)$_2$ based on the realistic two-dimensional five-orbital model. The U-VCs due to the AL processes are taken into account not only for the charge susceptibilities, but also for the superconducting gap equation. Based on the present beyond-ME formalism, the nodal s-wave state or fully gapped s_{++}-wave state is naturally obtained for a wide parameter range. The nodes appear only on the electron FSs at which the orbital character changes between $xz(yz)$ and xy. This result means the emergence of the loop nodes on the electron FSs, consistent with the theoretical prediction in Ref. [10]. In contrast, the gap functions on all hole FSs are always fully gapped, including the z^2-orbital outer hole FS. The obtained gap structure is consistent with the ARPES studies [7,8] and angle-resolved thermal conductivity measurement [37]. The obtained nodal s-wave state changes to a fully gapped s_{++}-wave state by introducing a small amount of impurities, accompanied by small reduction in $T_{\rm c}$.

The obtained results are essentially similar to the results of our previous RPA study [10] in which a phenomenological interorbital quadrupole interaction term was introduced to realize strong interorbital fluctuations in four d orbitals. In the present paper, it is confirmed that the following nontrivial

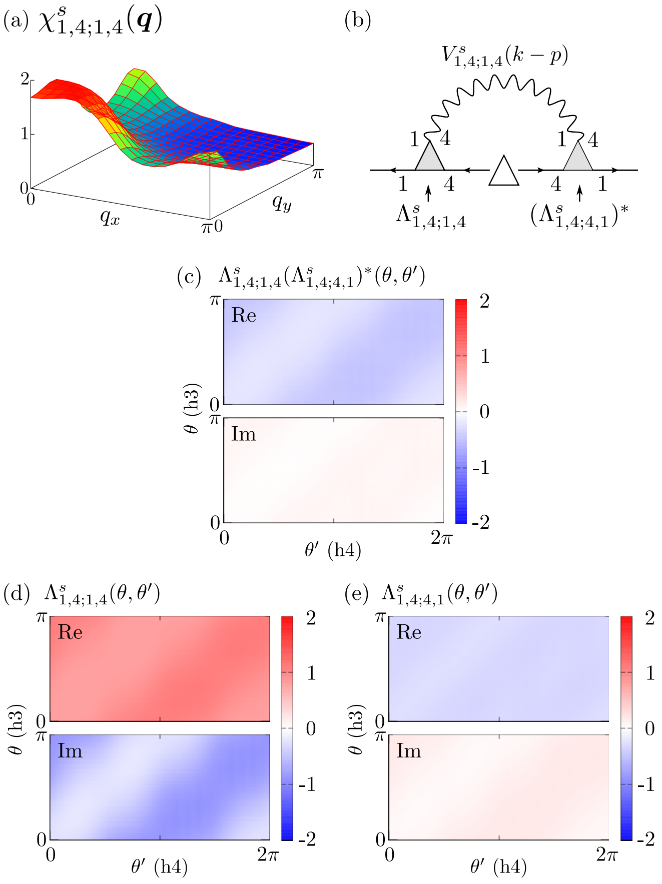

FIG. 13. The spin susceptibility $\chi^s_{1,4;1,4}(\boldsymbol{q})$. (b) The expression of the interaction given by $\chi^s_{1,4;1,4}(\boldsymbol{q})$. $V^s_{1,4;1,4}(\boldsymbol{q})$ is multiplied by $\Lambda^s_{1,4;1,4}(\Lambda^s_{1,4;4,1})^*$. (c) The real and imaginary parts of $\Lambda^s_{1,4;1,4}(\Lambda^s_{1,4;4,1})^*$. The red and blue colors, respectively, mean positive and negative interactions. Re$[\Lambda^s_{1,4;1,4}(\Lambda^s_{1,4;4,1})^*] < 0$ means that off-diagonal spin-channel U-VCs change the sign of the interaction given by $\chi^s_{1,4;1,4}(\boldsymbol{q})$. The real and imaginary parts of (d) $\Lambda^s_{1,4;1,4}$ and (e) $\Lambda^s_{1,4;4,1}$.

results are derived from the on-site Coulomb interaction by considering the U-VCs without introducing any phenomenological interaction terms: (i) Strong ferro-orbital and antiferro-orbital fluctuations associated with four d orbitals develop in Ba122 systems. (ii) A nearly isotropic gap function appears on all hole FSs, including the z^2-orbital FS. That is, the relation $\Delta_{h,z^2} \approx \Delta_{h,t_{2g}}$ holds. (iii) A nodal gap structure appears on the electron-type FSs, which corresponds to the loop node discussed in Ref. [10] for a wide parameter range. (iv) The obtained nodal s-wave state changes to the fully gapped s_{++}-wave state by introducing a small amount of impurities, accompanied by a small reduction in T_c. These obtained results satisfactorily explain the characteristic superconducting gap structure observed in Ba122 pnictides. The present gap equation beyond the standard ME formalism should be useful for understanding the rich variety of the superconducting states in various Fe-based superconductors, such as La1111 [23], FeSe [26], and Ba122 compounds.

ACKNOWLEDGMENTS

We are grateful to Y. Matsuda, T. Shibauchi, S. Shin, A. Fujimori, T. Shimojima, T. Yoshida, K. Okazaki, and S. Onari for fruitful discussions. This work was supported by a Grant-in-Aid for Scientific Research from the Ministry of Education, Culture, Sports, Science and Technology, Japan.

APPENDIX: THE REASON WHY SPIN FLUCTUATIONS MEDIATE ATTRACTIVE INTERACTION

In the main text, we showed the averaged $V_\Lambda^{(1)s}$ in Fig. 9(c). Interestingly, $\bar{V}_\Lambda^{(1)s}(\alpha,\beta)$ for $(\alpha,\beta) = (h1,h3)$, $(h2,h3)$, and $(h3,h4)$ are attractive, although their contribution to the pairing is very small. This nontrivial result originates from interorbital U-VCs for the spin channel since spin fluctuations always give repulsive interactions in the ME formalism. We explain the reason why spin fluctuations cause attractive interaction by focusing on $\bar{V}_\Lambda^{(1)s}(h3,h4)$.

Both $\chi^s_{1,1;1,1}(\boldsymbol{q})$ and $\chi^s_{1,4;4,1}(\boldsymbol{q})$ give repulsive interaction even if we consider the spin-channel U-VC because $V^s_{1,1;1,1}(\boldsymbol{q})$ and $V^s_{1,4;4,1}(\boldsymbol{q})$ are multiplied by $|\Lambda^s_{1,1;1,1}|^2 > 0$ and $|\Lambda^s_{1,4;1,4}|^2 > 0$, respectively. The sign is not changed, and therefore these spin fluctuations give repulsive interaction. In contrast, the sign of interaction caused by $\chi^s_{1,4;1,4}(\boldsymbol{q})$ [shown in Fig. 13(a)] is nontrivial. Figure 13(b) is the diagrammatic expression of the interaction given by $\chi^s_{1,4;1,4}(\boldsymbol{q})$. $V^s_{1,4;1,4}(\boldsymbol{q})$ is multiplied by $\Lambda^s_{1,4;1,4}(\Lambda^s_{1,4;4,1})^*$ of which the sign is nontrivial. In the present model, the real part of $\Lambda^s_{1,4;1,4}(\Lambda^s_{1,4;4,1})^*$ is negative as shown in the upper panel of Fig. 13(c). Due to the off-diagonal components of the spin-channel U-VC, the sign of interaction given by $\chi^s_{1,4;1,4}(\boldsymbol{q})$ is changed. The imaginary part of $\Lambda^s_{1,4;1,4}(\Lambda^s_{1,4;4,1})^*$ shown in the lower panel in Fig. 13(c) is canceled out by $\mathrm{Im}[\Lambda^s_{1,4;4,1}(\Lambda^s_{1,4;1,4})^*]$. We note that $\mathrm{Re}[\Lambda^c_{1,4;1,4}(\Lambda^c_{1,4;4,1})^*]$ is positive, thus the interaction given by interorbital charge susceptibility $\chi^c_{1,4;1,4}(\boldsymbol{q})$ is attractive. In Figs. 13(d) and 13(e), we show the real and imaginary parts of $\Lambda^s_{1,4;1,4}$ and $\Lambda^s_{1,4;4,1}$. $\mathrm{Re}[\Lambda^s_{1,4;1,4}(\Lambda^s_{1,4;4,1})^*]$ is given as $\mathrm{Re}[\Lambda^s_{1,4;1,4}]\mathrm{Re}[\Lambda^s_{1,4;4,1}] + \mathrm{Im}[\Lambda^s_{1,4;1,4}]\mathrm{Im}[\Lambda^s_{1,4;4,1}]$. The main contribution originates from $\mathrm{Re}[\Lambda^s_{1,4;1,4}]\mathrm{Re}[\Lambda^s_{1,4;4,1}]$ because $|\mathrm{Im}[\Lambda^s_{1,4;4,1}]| \ll 1$. For this reason, the pairing interaction caused by $\chi^s_{1,4;1,4}(\boldsymbol{q})$ is attractive due to the off-diagonal components of the spin-channel U-VC. The other attractive panels in Fig. 9(c) are understood in the same way.

---

[1] K. Kuroki, S. Onari, R. Arita, H. Usui, Y. Tanaka, H. Kontani, and H. Aoki, Phys. Rev. Lett. **101**, 087004 (2008).

[2] I. I. Mazin, D. J. Singh, M. D. Johannes, and M. H. Du, Phys. Rev. Lett. **101**, 057003 (2008).

[3] A. V. Chubukov, D. V. Efremov, and I. Eremin, Phys. Rev. B **78**, 134512 (2008).

[4] S. Graser, G. R. Boyd, C. Cao, H.-P. Cheng, P. J. Hirschfeld, and D. J. Scalapino, Phys. Rev. B **77**, 180514(R) (2008); T. A. Maier, S. Graser, P. J. Hirschfeld, and D. J. Scalapino, *ibid.* **83**, 220505(R) (2011).

[5] H. Kontani and S. Onari, Phys. Rev. Lett. **104**, 157001 (2010).

[6] K. Suzuki, H. Usui, and K. Kuroki, J. Phys. Soc. Jpn. **80**, 013710 (2011).

[7] T. Shimojima, F. Sakaguchi, K. Ishizaka, Y. Ishida, T. Kiss, M. Okawa, T. Togashi, C.-T. Chen, S. Watanabe, M. Arita, K. Shimada, H. Namatame, M. Taniguchi, K. Ohgushi, S. Kasahara, T. Terashima, T. Shibauchi, Y. Matsuda, A. Chainani, and S. Shin, Science **332**, 564 (2011).

[8] T. Yoshida, S. Ideta, T. Shimojima, W. Malaeb, K. Shinada, H. Suzuki, I. Nishi, A. Fujimori, K. Ishizaka, S. Shin, Y. Nakashima, H. Anzai, M. Arita, A. Ino, H. Namatame, M. Taniguchi, H. Kumigashira, K. Ono, S. Kasahara, T. Shibauchi, T. Terashima, Y. Matsuda, M. Nakajima, S. Uchida, Y. Tomioka, T. Ito, K. Kihou, C. H. Lee, A. Iyo, H. Eisaki, H. Ikeda, R. Arita, T. Saito, S. Onari, and H. Kontani, Sci. Rep. **4**, 7292 (2014).

[9] Y. Zhang, Z. R. Ye, Q. Q. Ge, F. Chen, J. Jiang, M. Xu, B. P. Xie, and D. L. Feng, Nat. Phys. **8**, 371 (2012).

[10] T. Saito, S. Onari, and H. Kontani, Phys. Rev. B **88**, 045115 (2013).

[11] C. Fang, H. Yao, W.-F. Tsai, J. Hu, and S. A. Kivelson, Phys. Rev. B **77**, 224509 (2008).

[12] R. M. Fernandes, A. V. Chubukov, J. Knolle, I. Eremin, and J. Schmalian, Phys. Rev. B **85**, 024534 (2012).

[13] F. Krüger, S. Kumar, J. Zaanen, and J. van den Brink, Phys. Rev. B **79**, 054504 (2009).

[14] C.-C. Lee, W.-G. Yin, and W. Ku, Phys. Rev. Lett. **103**, 267001 (2009).

[15] S. Onari and H. Kontani, Phys. Rev. Lett. **109**, 137001 (2012).

[16] H. Kontani and Y. Yamakawa, Phys. Rev. Lett. **113**, 047001 (2014).

[17] Y. Yamakawa, S. Onari, and H. Kontani, Phys. Rev. X **6**, 021032 (2016).

[18] S. Onari, Y. Yamakawa, and H. Kontani, Phys. Rev. Lett. **116**, 227001 (2016).

[19] Y. Yamakawa and H. Kontani, Phys. Rev. Lett. **114**, 257001 (2015).

[20] M. Tsuchiizu, Y. Yamakawa, and H. Kontani, Phys. Rev. B **93**, 155148 (2016).

[21] S. Sachdev and R. La Placa, Phys. Rev. Lett. **111**, 027202 (2013).

[22] Y. Wang and A. Chubukov, Phys. Rev. B **90**, 035149 (2014).

[23] S. Onari, Y. Yamakawa, and H. Kontani, Phys. Rev. Lett. **112**, 187001 (2014).

[24] R. Tazai, Y. Yamakawa, M. Tsuchiizu, and H. Kontani, Phys. Rev. B **94**, 115155 (2016).

[25] R. Tazai, Y. Yamakawa, M. Tsuchiizu, and H. Kontani, J. Phys. Soc. Jpn. **86**, 073703 (2017).

[26] Y. Yamakawa and H. Kontani, Phys. Rev. B **96**, 045130 (2017).

[27] T. Miyake, K. Nakamura, R. Arita, and M. Imada, J. Phys. Soc. Jpn. **79**, 044705 (2010).

[28] M. Ishikado, K. Kodama, R. Kajimoto, M. Nakamura, Y. Inamura, S. Wakimoto, A. Iyo, H. Eisaki, M. Arai, and S. Shamoto, Physica C **471**, 643 (2011).

[29] F. L. Ning, K. Ahilan, T. Imai, A. S. Sefat, M. A. McGuire, B. C. Sales, D. Mandrus, P. Cheng, B. Shen, and H.-H. Wen, Phys. Rev. Lett. **104**, 037001 (2010).

[30] K. Kitagawa, N. Katayama, K. Ohgushi, M. Yoshida, and M. Takigawa, J. Phys. Soc. Jpn. **77**, 114709 (2008).

[31] R. M. Fernandes, L. H. VanBebber, S. Bhattacharya, P. Chandra, V. Keppens, D. Mandrus, M. A. McGuire, B. C. Sales, A. S. Sefat, and J. Schmalian, Phys. Rev. Lett. **105**, 157003 (2010)

[32] M. Yoshizawa, D. Kimura, T. Chiba, S. Simayi, Y. Nakanishi, K. Kihou, C.-H. Lee, A. Iyo, H. Eisaki, M. Nakajima, and S. Uchida, J. Phys. Soc. Jpn. **81**, 024604 (2012).

[33] T. Goto, R. Kurihara, K. Araki, K. Mitsumoto, M. Akatsu, Y. Nemoto, S. Tatematsu, and M. Sato, J. Phys. Soc. Jpn. **80**, 073702 (2011).

[34] A. E. Böhmer, P. Burger, F. Hardy, T. Wolf, P. Schweiss, R. Fromknecht, M. Reinecker, W. Schranz, and C. Meingast, Phys. Rev. Lett. **112**, 047001 (2014).

[35] J. S. Kim, P. J. Hirschfeld, G. R. Stewart, S. Kasahara, T. Shibauchi, T. Terashima, and Y. Matsuda, Phys. Rev. B **81**, 214507 (2010)

[36] Y. Wang, J. S. Kim, G. R. Stewart, P. J. Hirschfeld, S. Graser, S. Kasahara, T. Terashima, Y. Matsuda, T. Shibauchi, and I. Vekhter, Phys. Rev. B **84**, 184524 (2011).

[37] M. Yamashita, Y. Senshu, T. Shibauchi, S. Kasahara, K. Hashimoto, D. Watanabe, H. Ikeda, T. Terashima, I. Vekhter, A. B. Vorontsov, and Y. Matsuda, Phys. Rev. B **84**, 060507(R) (2011).

[38] D. V. Efremov, M. M. Korshunov, O. V. Dolgov, A. A. Golubov, and P. J. Hirschfeld, Phys. Rev. B **84**, 180512(R) (2011).

[39] A. Kawabata, S. C. Lee, T. Moyoshi, Y. Kobayashi, and M. Sato, J. Phys. Soc. Jpn. **77**, 103704 (2008); M. Sato, Y. Kobayashi, S. C. Lee, H. Takahashi, E. Satomi, and Y. Miura, *ibid.* **79**, 014710 (2010); S. C. Lee, E. Satomi, Y. Kobayashi, and M. Sato, *ibid.* **79**, 023702 (2010).

[40] Y. Nakajima, T. Taen, Y. Tsuchiya, T. Tamegai, H. Kitamura, and T. Murakami, Phys. Rev. B **82**, 220504(R) (2010).

[41] J. Li, Y. Guo, S. Zhang, S. Yu, Y. Tsujimoto, H. Kontani, K. Yamaura, and E. Takayama-Muromachi, Phys. Rev. B **84**, 020513(R) (2011).

[42] K. Kirshenbaum, S. R. Saha, S. Ziemak, T. Drye, and J. Paglione, Phys. Rev. B **86**, 140505 (2012).